UNIVERSITÀ DEGLI STUDI DI PADOVA

Dipartimento di Fisica e Astronomia “Galileo Galilei”

Corso di Laurea in Astronomia

Tesi di Laurea

Analysis of fractures in crater floors: the case of Ceres

Relatore

Prof. Monica Lazzarin

Correlatore

Dr. Alice Lucchetti

Laureando

Marco Baroni

Anno Accademico 2018/2019

Analysis of fractures in crater floors: the case of Ceres

Marco Baroni

Anno Accademico 2018/2019

Abstract

This study is focused on Floor Fractured Craters (FFCs) located on Ceres, a particular category of craters with nets of fractures on their floors. In this work we analyze the orientation and the length distribution of the fractures present on the craters' floors of Dantu and Occator. We find that for each crater the fractures have a preferential orientation and , hence, they are not randomly distributed. In addition, the fractures length frequency distribution analysis reveals that some fractures can penetrate the entire shell of Ceres. This interesting result means that these fractures can serve as conduits for cryovolcanic activity. This analysis provides preliminary results regarding fractures behavior on Ceres surface and will be useful for additional future analyses.

Sommario

Questo studio è focalizzato su una particolare tipologia di crateri, localizzati su Cerere, denominati Crateri dal Fondo Fratturato. In questo lavoro abbiamo analizzato l'orientazione e la distribuzione delle lunghezze delle fratture presenti sui fondi dei crateri Dantu e Occator. Si è trovato che, per ogni cratere, le fratture non sono casualmente distribuite, ma hanno una direzione di orientamento preferenziale. Inoltre, l'analisi della distribuzione in frequenza delle lunghezze delle fratture, rivela che alcune di queste posso penetrare interamente la crosta di Cerere. Questa conclusione è di estremo interesse, poichè significa che queste fratture possono agire da "condotto" per attività criovulcaniche. Questa analisi ha riportato risultati preliminari riguardanti il comportamento delle fratture su Cerere, e sarà utilizzato per ulteriori analisi che verrano fatte nel prossimo futuro.

Contents

Chapter 1

Introduction

On the 6th of March 2015, after a 14-month long mission around Vesta, the Dawn spacecraft arrived at Ceres, giving the first opportunity to study from near this unique celestial body.
The probe remained in orbit around Ceres until the 1st of November 2018, when it ended all of its fuel, remaining in uncontrolled orbit around the dwarf planet. Over these 3 years, 7 months and 26 days in orbit around Ceres, Dawn produced more than 100 GB of data, thus reporting the most detailed view that we have ever had of this dwarf planet in more than 200 years from its discovery.

Between the different features observed on the surface of Ceres, we focused our attention on two peculiar impact craters, Dantu and Occator. These two craters are included in a particular category of craters called FFCs (Floor Fractured Craters) that present some peculiar characteristics when compared to normal craters. Indeed, they present wide nets of fractures on their floors.

Specifically, we characterize the fractures pattern deriving: (I) size-frequency distribution of fractures length to understand if fractures can penetrate the entire shell thickness of Ceres and (II) Rose diagram to determine if a preferential orientation of these fractures exists.

Chapter 2

Ceres and the Dawn mission

2.1 Ceres

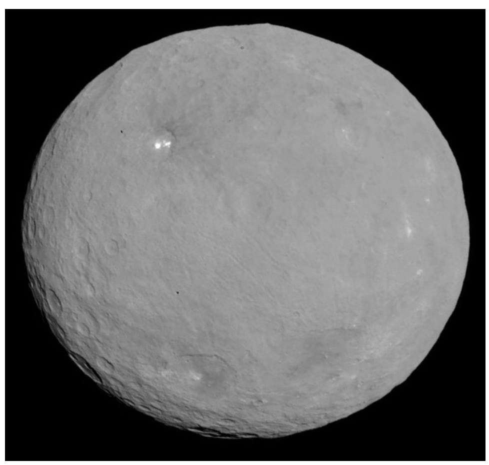

Figure 2.1: Ceres as seen by the Dawn spacecraft on the 6th of May 2015 from 13,600 km, it's visible the bright spot, named "spot 5" in the Occator crater. Credits: NASA/JPL-Caltech/UCLA/MPS/DLR/IDA.

Ceres, discovered in 1801 by the Italian astronomer Giuseppe Piazzi, is the closest, to Earth, dwarf planet in the Solar System. With a radius of about 476 km, it is the most massive object in the Main Asteroid Belt.
Ceres' sidereal period is about 4.60 years with an orbit that is inclined by 10.593 deg, with respect to the ecliptic. It has an eccentricity of 0.075, and its average distance from the Sun is 2.8 AU. It rotates around its axis, which is inclined by

4.00 deg, completing one rotation every 9.07 hours.
Before 2006, when it was 'upgraded' to the status of dwarf planet, it was classified as a C-type asteroid meaning that it contains high percentages of Carbon, either in elementary or molecular forms, especially clustered in a type of rock called carbonaceous chondrite. Its surface acceleration of gravity is about 0.28 m/s^2 (Hisinger et al. 2016).
Moreover, Ceres is a unique example of volatile-rich dwarf planet (Fu et al. 2017) and its crust is mechanically strong (the maximum effective viscosity should be around 10^{25} Pa s). This rheology suggests a crustal composition of carbonates, phyllosilicates and water ice (less than 25 volume percent) in addition to a 30% volume of low-density, high-strenght materials, probably made by salt and/or clathrate hydrates. The latter are concentrated in a probably 41 km thickness crust with a total average density of 1287 kg/m^3 (Fu et al. 2017). Ammonia could also be part of the composition of the crust, indeed, there were found traces of ammonia bounded to the phyllosilicates (Buczkowski et al. 2018). One of Ceres distinct features are the many bright spots, named faculae, that are probably made of various salts as magnesium sulfate and/or sodium carbonate (DeSanctis et al., 2016).
Furthermore, as normal for planetoids in an region like the main belt, Ceres surface is constellated by craters of various sizes and morphologies, but there are not craters larger than 280 km. This is a peculiar aspect of Ceres since it is at least 4.5 billion years old. The most plausible hypothesis for the lack of large impact craters is the presence of somehow geological activity that flattened and, maybe, is flattening the surface, making the bigger craters disappeared over time.
A possible candidate for this kind of geological activity is the viscous relaxation. Indeed, considering that the surface temperature ranges between 120 K (at high latitudes) and 150-160 K (at low latitudes), the ice is not strong enough to retain large-scale topography. Hence, the bigger craters are expected to flatten out on relatively short geological timescales (Bland et al. 2016). Another hypothesis is attributed to cryo-volcanism, due to both the presence of some traces of water-ice material in the crust, and flow features on the surface (Krohn et al. 2016). Moreover, the salts observed within the faculae are hypothesized as the result of this cryo-volcanic activities.
Previous works suggest that Ceres crust is quiet heterogeneous, indeed, the features that lead to the presence of water ice-salt mixture, such as ring-mold craters (Krohn et al. 2018), are not evenly distributed on the surface. Thus leading to the presence of complex geological crustal structure (Bland et al., 2016).
From the evidences reported above, it has been suggested that Ceres possibly had a global or partial ocean in the past. The freezing of this ocean could have lead to the crustal salts accumulation that are seen today (Fu et al., 2017).
For this reason, Ceres is thought to be partially differentiated having both a crust and a mantle.
The latter should extend below the crust (nearly 41 km deep) to near the center, for a total of 428.8 km. The mantle is thought to be rich in silicate and is

mechanically weak with maximum viscosity of almost 10^{21} Pa s in the uppermost part. This suggests the presence of liquid pore fluids in this region (the first 60 km thickness) that avoided igneous differentiation (Fu et al. 2017) and remained brittle and enriched with other substances. From a geomorphological point of view, Ceres is known to be a geological complex dwarf planet with many different features on its surface, such as faculae, many different crater morphologies (Hisinger et al. 2016), chains of pits, as the Samhain Catenae (Scully et al. 2017), and the presence of the Ahuna Mons, whose height is about 4 km. Among the different geomorphological features observed on the surface of Ceres, this work focuses on the so-called Floor Fractured Craters, FFCs, such as Dantu and Occator craters (see Chapter 3).

Mean radius [km]	476
Sidereal period [yr]	4.60
Orbital inclination [°]	10.593
Eccentricity [ ]	0.075
Average Sun distance [AU]	2.8
Axis inclination [°]	4.00
Rotational period [h]	9.07
Acceleration of gravity [m/s^2]	0.28

Table 1.1 : Physical parameters of Ceres.

2.2 Dawn mission

Dawn is a spacecraft launched on the 27th of September 2007 with the objective of study the asteroid Vesta and the dwarf planet Ceres. It arrived on the dwarf planet on the 5th of March 2015 and stayed in orbit around it up until the 1st of November 2018, effectively prolonging the mission that was scheduled to end on June 2016. The core of the probe is a graphite composite cylinder, which is surrounded by aluminium panels on which most of the hardware is fixated. On this part of the spacecraft are also mounted the heaters that controls the probe temperature (Dawn at Ceres, press kit NASA).

Figure 2.2: The logo of the Dawn mission. Credits: NASA.

Its main characteristics are:

- 1.64 meters long, 1.27 meters wide and 1.77 meters high spacecraft (solarsystem.NASA.gov).
- An high-gain antenna of 1.52 meters by diameter used for primarly communications with Earth, in addition to three other low-gain antennas used when the principal one is not pointing at Earth (Dawn at Ceres, press kit NASA).

- A solar array 20 meters long (36.4 m^2 of total surface area), (solarsystem.NASA.gov).
- Weight of 747.1 kg with an addition of 425 kg of xenon propellent and other 45.6 kg of hydrazine fuel, (solarsystem.NASA.gov).
- Two 8.3x2.3 meter solar arrays, together providing 1.4 kW at Dawn maximum distance from the Sun, with the energy storage that was a 35 A/h rechargeable Ni-H battery, (solarsystem.NASA.gov).
- Three 33x41 cm cylindrical ion thrusters movable in two axes, providing a thrust of 19 to 91 mN, each unit weights 8.9 kg. Only one thruster at time was used during the mission (Dawn at Ceres, press kit NASA).

This propulsion system accelerated the spacecraft, at full thrust, from 0 to 26.8 m/s in 4 days, resulting in the record for the highest variation of velocity in less time for a probe, (solarsystem.NASA.gov). The thrusters work by using an electrical charge to accelerate ions from the Xenon fuel, that was chosen for it's chemical unreactivity and atomic weight, to a speed 7 to 10 times that of conventional chemical engines (Dawn at Ceres, press kit NASA). This propulsion consumed only 3.25 mg/s of Xenon at full power (Dawn at Ceres, press kit NASA).

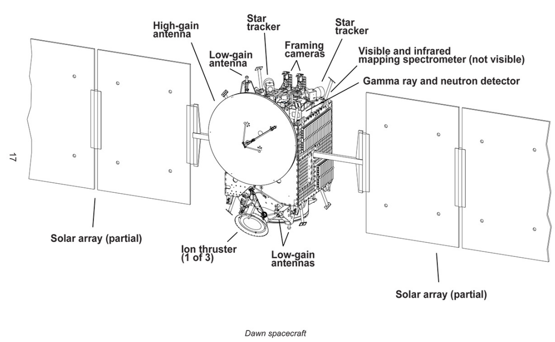

Figure 2.3: Schematic structure of the Dawn spacecraft.Credits: NASA.

The payload onboard Dawn is composed by the following instruments:

- A Gamma Ray and Neutron Detector (GRaND), consisting in a total of 21 sensors with a wide field of view capable of detecting the possible emanations of those particles from the surface of the two celestial bodies, allowing to study the composition of the surface up to 1 m in the crust (Dawn at Ceres, press kit NASA).

- A Visual and Infrared Imaging Spectrometer (VIR), this instrument was used to study the surface mineralogy of Vesta and Ceres, each measurement recorded the light intensity at more than 400 wavelenght ranges in each pixel (Dawn at Ceres, press kit NASA).

- Two Framing Cameras (FC), this instrument acquired images of the surface of Ceres that were used for this study, (for more information see section 1.2.1).

The Dawn spacecraft was the first spacecraft orbiting two separate bodies in only one mission and studying both a dwarf planet and an asteroid.

2.2.1 Framing Cameras

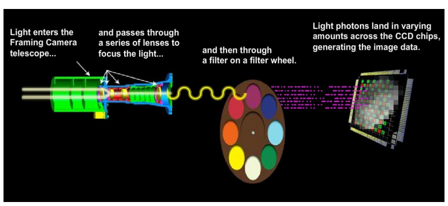

Figure 2.4: Schematized functioning of the Frame Cameras.
Credits: NASA.

The Framing Camera (FC) is the German contribution to the Dawn mission and allowed the deep study of the physical parameters of Ceres, as well as the reconstruction of its global shape, local topography and surface geomorphology. Moreover, the data provided important informations on the surface composition of Ceres.
The two cameras are perfectly identical, they weight 5.5 kg, have a 19 mm aperture size, a focal length of 150 mm and an Instantaneus Field Of View (IFOV) of 93.3 μrad. The cameras mounted refractive optics that focus the light on a filter wheel equipped with one clear filter (ranging from 400 to 1100 nm (Hisinger et al. 2016)), and seven band-pass filters that covers the wavelengths from visible to near-IR (438, 555, 653, 749, 829, 917 and 965 nm (Hisinger at al. 2016), (see table 1.2 for more details). Then, the filtered light is transmitted to a a 1024x1024 frame transfer CCD (Mastrodemos et al.). To correct and compensate the aberrations were used the following precautions:

- Chromatic aberration was compensated chosing a crown glass, with positive refracting power, for the first lens, followed by two flint glass, with negative refracting powers, then again followed by another flint lens with poitive refracting power (Sierks et al. 2011).

- Spherical aberration was corrected with an aspherical first lens surface (Sierks et al. 2011).

- All the aberrating effect that derives from temperature changings (for example a change in the focal length), were dealt by mounting the two central lenses in an inner barrel with a different thermal expansion coefficient than the outer one. This allowed to keep the focal plane within a range of 30 μm (Sierks et al. 2011).

The optical system is located in a lens barrel mounted on the camera's head, and all the structure is reinforced with braces from the head to the base of the camera, where the buffle resides (Sierks et al. 2011).
The calibration was done during the flight, (when the cameras were also used for it's navigation, as well during the voyage phase and the orbit phase). Photometric calibrations imaged Vega and various solar analogs, while geometric calibrations used cluster observations to estimate the focal length. The calibration results allowed an astrometric accuracy of 0.09 - 0.11 pixels (1-σ) when imaging a few stars at a minimum signal-to-noise (SNR) > 10 (Mastrodemos et al.).
For estimating the camera's alignment in the body frame were again used the cluster observation, leading to a residual pointing error of $\sim$1 FC pixel, that is considerably random (Mastrodemos et al.).

The resolution of the Framing Camera was up to 62 m per pixel in low altitude mapping orbit (LAMO), at an angular resolution of 93.7 μrad/px (Mastrodemos et al.). To protect the optical system the cameras use a resealable front door that, when open, elevates the total height of the cameras to 422 mm (Sierks et al. 2011). The total power consumption in nominal operation was of 17 W (Sierks et al. 2011).
At the end of the camera head, there are the filter wheel, the CCD and the electronics for the operations of the CCD. After the head there is the electronics box, or E-box, where the Data Processing Unit, the Power Converter Unit and the Mechanism Control Unit are situated, and they are thermally insulated from the camera head (Sierks et al. 2011). All the components are insulated from external sunlight and temperature with a Multi-Layer Insulation, or MLI (Sierks et al. 2011). Thanks to Doppler measurements of the orbiting Dawn and observations of characteristic landmarks, the FCs measured the rotation rate, the orientation of the spin axis, the mass, the gravity field, the shape, the volume and the bulk density of Ceres. Thanks to the huge amount of images acquired, it was possible to obtain mosaics of the entire surface of Ceres, in addition to to a Digital Terrain Model (DTM) produced by the stereophotogrammetry technique with a vertical accuracy of 12 m.

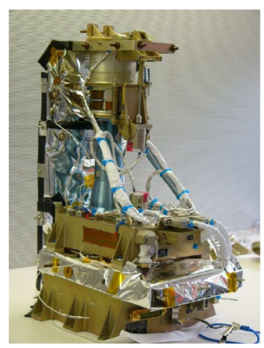

Figure 2.5: The Framing Camera without the MLI.
Credits: Sierks et al. 2011.

Item	**Specification**
Focal Lenght	150 mm
Focal shift	< 20 μm
Field of view	5.5 ° X 5.5 °
IFOV	93.7 μrad
Field Curvature	< 10 μm
Distortion	<0.1%
Spectral Range	400 - 1050 nm
Spectral Transmission	> 75 %

Table 2.1: Optical specifications of the FC. Credits: Sierks et al. 2011

Center λ [nm]	**Bandwidth [nm]**	**Transmission [%]**	**Thickness [mm]**
polychromatic	450 ± 10 - 920 ± 10	98	6.00 ± 0.05
430 ± 2	40 ± 5	> 75	2.00 ± 0.05
550 ± 2	40 ± 5	> 75	5.90 ± 0.05
650 ± 2	40 ± 5	> 75	6.60 ± 0.05
750 ± 2	40 ± 5	> 75	6.40 ± 0.05
830 ± 2	40 ± 5	> 75	5.90 ± 0.05
920 ± 2	40 ± 5	> 75	5.30 ± 0.05
980 ± 2	80 ± 5	> 75	4.80 ± 0.05

Table 2.2: Tabulated philters specifications. Credits: Sierks et al. 2011

Chapter 3

Floor Fractured craters analysis

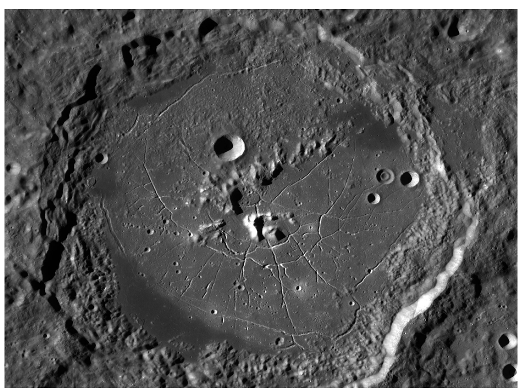

Figure 3.1: The Humboldt crater on the Moon, a typical example of FFC-I. Credits: NASA, Lunar Recoinnaissance Orbiter (LRO).

Floor Fractured Craters (FFCs) are craters with peculiar nets of fractures on their floor. This type of crater was firstly found on the Moon and then on other bodies, like Mars and Ceres. The fractures systems are present in various form on the craters, they can cut the floor radially, from the center to the outer parts, or can be disposed in concentric patterns around the crater center (Buczkowski et al. 2018).
Another important parameter for characterizing FFCs is the depth to diameter, d/D, ratio. Indeed, lunar FFCs are shallower when compared to normal lunar craters. Cerean FFCs also show shallower craters floor when comparing FFCs to normal craters (Buczkowski et al. 2018).

There are various typologies of FFCs, divided in the following classes:

- **Class I**: Radial and/ or concentric features, central peak complexes.
- **Class II**: Uplifted central region, concentric region.
- **Class III**: Wide moat between wall and interior, radial and/or polygonal fractures.
- **Class IV**: Characterized by a V-shaped moat, and divided in three categories:
  - **IVa**: Radial or concentric features, convex up floor profile.
  - **IVb**: Pronounced inner ridge on the interior side, subtle fractures, irregular convex up profile.
  - **IVc**: Hummocky interior.
- **Class V**: Degraded crater walls, radial and/of polygonal fractures.
- **Class VI**: Mare-flooded interiors, concentric fracture pattern near walls.

(Schultz 1976, Jozwiak et al. 2012, 2015).

This classification is based on the observation of lunar FFCs and can be applied to other bodies. Indeed, on the surface of Ceres there are the FFC Class I and Class IV with all of their subtypes (Buczkowski et al. 2018). This is because the cerean FFCs are relatively young and do not have the heavily degraded walls associated with Class 5 FFCs. Moreover, Cerean FFC have both the radially cutting fractures and the concentric cutting fractures. In addition, they do not have concave-up profiles at their centers or mare-flooded interiors, hence, Class 2 and 6 are excluded on Ceres (Buczkowski et al. 2018). The two craters analyzed in this work, Dantu and Occator, are classified as Class I floor fractured crater. The fractures are an important object of study in planetary sciences because their origin can be related to volcanic, cryo-volcanic or some sort of geological activity that can cause processes like viscous relaxation or floor uplifting (Buczkowski et al. 2018). Indeed, they can serve as fluid conduits bringing the subsurface material to the surface. Therefore, the study of the distribution of fractures on a planetary body can be a tool to infer the thickness of the fractured crust (Lucchetti et al., 2017).
Understanding the origin of fractures can provide information about the Ceres crustal and/or sub-crustal composition, as well as the possible existence of geological acitvity on the body (Buczkowski et al. 2018).

The importance of studying the fractures distribution lies in the fact that fractures following an exponential-kind distribution are thought to not penetrate too deep in the crust, hence, they are not involved in the resurfacing of deep-crust material. On the other hand, those fractures following a powerlaw-kind distribution are thought to be related with fractures that penetrate the entire crust (Mazzarini and D' Orazio, 2003; Mazzarini, 2004; Soliva and Schultz, 2008; Mazzarini and Isola, 2010).

From this consideration, we can make a differentiation in the distribution of fractures, leading to two main typologies:

- 1. Localized fractures systems that presents few large fractures that cuts deep in the crust and down to the mechanical discontinuity.
  Those presents a distribution of length that follows a powerlaw:

  $$N(> l) = cl^{-\alpha} \tag{3.1}$$

  Where N(>l) is the number of fractures with length more than a value l, c is a scale factor and α is the exponent of the power law that identify the slope of the log-log graph.

- 2. Distributed fracture systems that are almost evenly spaced. These fractures are confined within a specific layer of the crust and does not grow down to the main discontinuity.
  They present a distribution of length that follows an exponential law:

  $$N(> l) = \beta e^{-\lambda\alpha} \tag{3.2}$$

  Where N(>l) is, again, the number of fractures with length more than a value l, β and λ are parameters for the exponential and α is, again, is the exponent of the exponential that characterize the slope of the plotted line on the log-log graph.

For this reason it is important to study Floor Fractured Craters, especially in case of the dwarf planet Ceres. Indeed, in light of its geological complexity and almost non-uniform surface morphology, the fractures analysis can give unique insights on the origin and evolution of this dwarf planet.

3.1 Dantu crater

The Dantu crater, located at coordinates 24.3°N 138.2°E in the Vendimia Planitia depression in the northern hemisphere of Ceres, is 120 km in diameter. It shows remnants of a central peak and a wide and flat floor (Kallisch et al. 2017), with a medium depth of 4.4 km (Buczwkowski et al. 2018).
Its age is thought to be 230 ± 30 Myr that was derived using an ejecta blanket counting model, even if the crater density lowers significantly when reaching the crater floor, indicating a younger surface age (Kallisch et al. 2017). Since there are no indications that melting events occurred in the past, the younger surface is probably caused by debris avalanches and granular flows, that filled up the center of the crater (Kallisch et al. 2017).
Dantu shows a prominent system of fractures, almost all located in the southern portion of the crater (see chapter 2.1 for details), and some of those fractures are associated with bright spots (Kallisch et al. 2017).
Those bright spots are relatively abundant on the crater floor. There are more then 80 with diameters between 100 and 500 m and a few other that are about 1

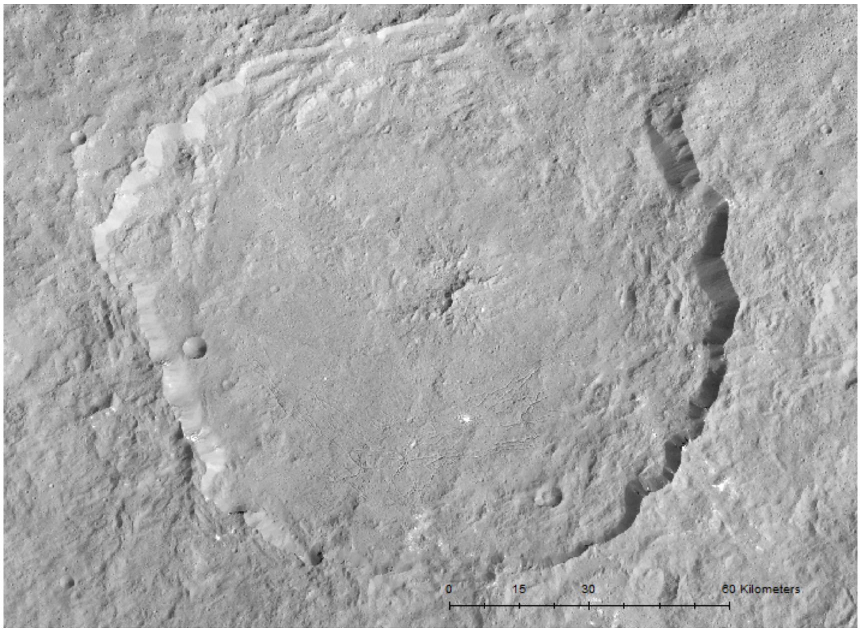

Figure 3.2: The Dantu crater.
In the image it is well visible the central peak, as well as some of the bright spots in the southern region.
The North is in the upperward direction.
Credits :

km in diameter. Moreover, most of the bright spots are located in the southern part of the crater, and within a 10.5 x 9 km area, causing an increment in the local albedo (Kallisch et al. 2017).
This southern area of the crater is on average 1 km higher in elevation compared to the northern crater floor (Kallisch et al. 2017). The Dawn spacecraft performed also a spectral analysis of the Dantu revealing a strong absorption around 2.7 μm, associated with structural OH-groups in phyllosilicates, around 3.1 μm, likely due to ammoniated phyllosilicates, and around 3.9 μm, consistent with carbonate phases (Kallisch et al. 2017). Some other absorption around 3.2-3.5 μm and 4.2 μm were observed, but their origin is not yet understood (Kallisch et al. 2017).
In synthesis, Dantu is a diverse complex crater, showing non-uniformly distributed features like fracture systems, a high number of small bright spots, an asymmetric floor profile, uneven distributed spectral properties and an irregular ejecta distribution (Kallisch et al. 2017).

Coordinates	Diameter	Depth
24°18'00"N ; 138°13'48"E	120 km	4.4 km

Table 2.1: Parameters of the Dantu crater (Buczwkoski et al. 2018).

3.2 Occator crater

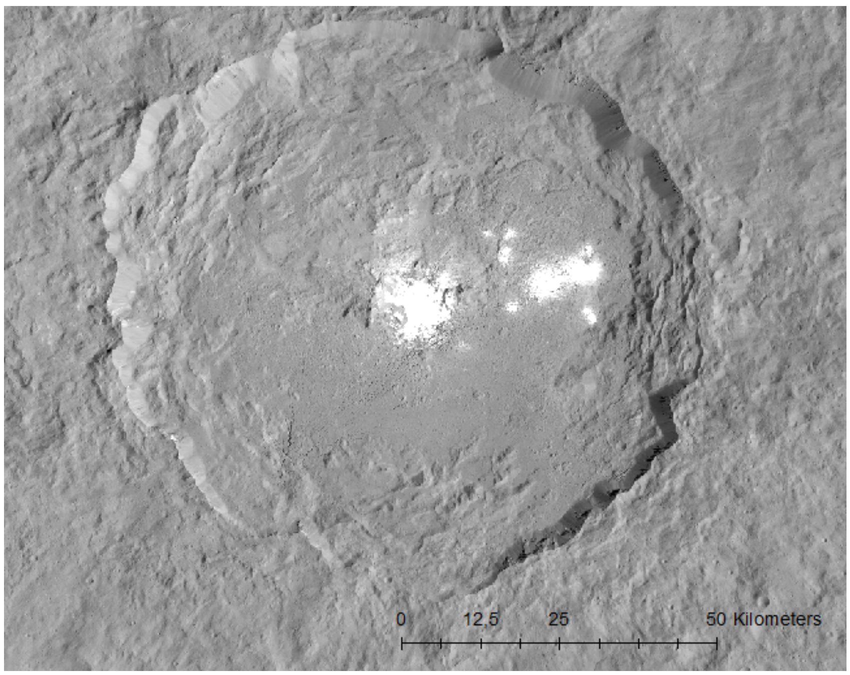

Figure 3.3: The Occator crater.
In the image the Ceralia Facula at the center and the Vinalia Faculae in the eastern part of the crater are shown.
The North is in the upperward direction
Credits :

The Occator crater, located at coordinatesd 19.8°N, 239.3°E near the Hanami Planum, in the Occator Quadrangle, is 92 km in diameter and 4.3 km in depth (Buczkowski et al. 2018). Its central pit is 9 km wide and almost 1 km deep, with a 2 km wide and 400 m high central dome on its floor (Schenk et al., 2015; Hiesinger et al., 2016; Buczkowski et al., 2016). The floor material on Occator ranges from smooth to knobby, but in the northeast is overlain by lobate flows, thought to be emanated from the center of the crater (Krohn et al. 2016).
The floor of Occator is extensively fractured, with type of fractures ranging from linear fractures in the northeastern part to concentric fractures around the central pit and around the crater wall (see chapter 2.1 for details), (Buczkowski

et al., 2018).
Associated with the fractures there are the faculae, or "bright spots". These high albedo surface features are relatively abundant on the cerean surface, but the Occator crater hosts the highest number of them, as well as the biggest one, the Ceralia Facula which is visible in the central part of the crater and it is associated with the dome within the central pit (Buczkowski et al., 2018). Other smaller faculae are the Vinalia Faculae which are located in the north-east part of the crater and associated with the fractures cutting the lobate flows (Buczkowski et al., 2018).
The faculae on Occator are composed almost entirely by sodium carbonates (DeSanctis et al. 2016).

Coordinates	**Diameter**	**Depth**
19°49'12"N ; 239°19'48"E	92 km	4.3 km

Table 2.2: Parameters of the Occator crater (Buczwkoski et al. 2018).

3.3 Dataset and Methods

The dataset consists in the fractures located on the crater floors of Occator and Dantu. The mapping of these fractures was done using the HAMO (High Altitude Mapping Orbit) and LAMO (Low Altitude Mapping Orbit) maps. Those two maps are mosaics made with the images that the FCs cameras acquired during the Dawn mission. We use also the DTM (Digital Terrian model) that provide information about the elevation of the features. The DTM has a vertical accuracy of 12 m, while the LAMO map has a resolution of 20 m/px.
The DTM was done during the HAMO phase, at an altitude of about 1475 km (astrogeology.usgs.gov), during which the FCs acquired about 2350 images of the surface of Ceres in clear filter (Preusker et al. 2016). To produce the DTM, the images taken at different angles and with similar illumination conditions, were combined using a method called stereophotogrammetry (SPG) (Preusker et al. 2016). We used the DTM to understand the elevation of the different areas we mapped.

The mapping of the fractures was done using the Arcgis software ArcMap. On the LAMO map the fractures were mapped as polylines, modeled as geometrical lines connected by their vertexes. We calculated the length of fractures and the x and y coordinates of the starting point, the ending point and the midpoint of each fracture. These parameters were extrapolated in a txt file, that was then used in Python with the numpy command genfromtxt.
The total amount of fractures is 1462, 630 on Dantu and 832 on Occator. (for the complete index of the single fracture lengths see Appendix B).

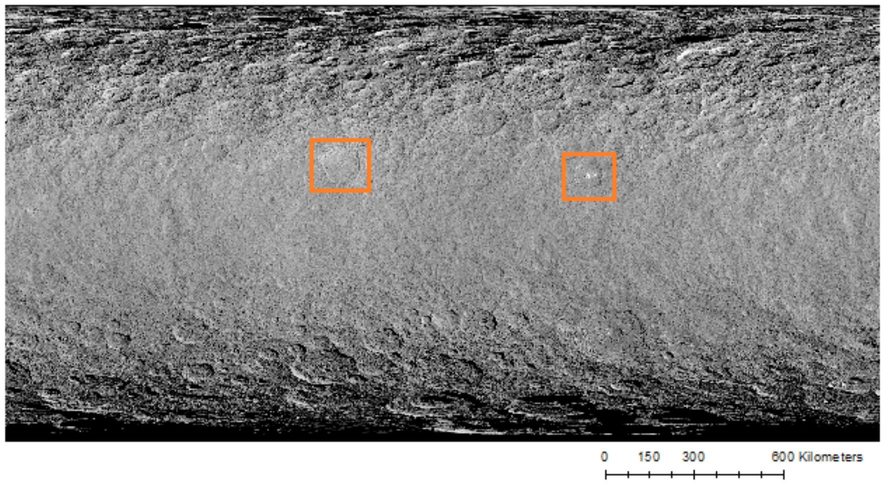

Figure 3.4: The LAMO mosaic of the surface of Ceres.
The two orange rectangles highlight the two craters under study, Dantu and Occator.
Credits: .

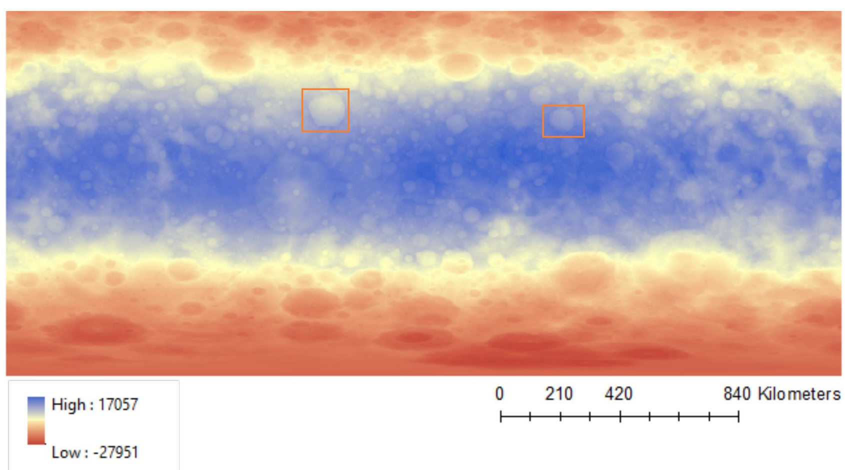

Figure 3.5: The DTM produced using images from the HAMO map acquired by the FCs cameras onboard the Dawn spacecraft.
The two orange rectangles highlight the two craters under study, Dantu and Occator .
Credits: .

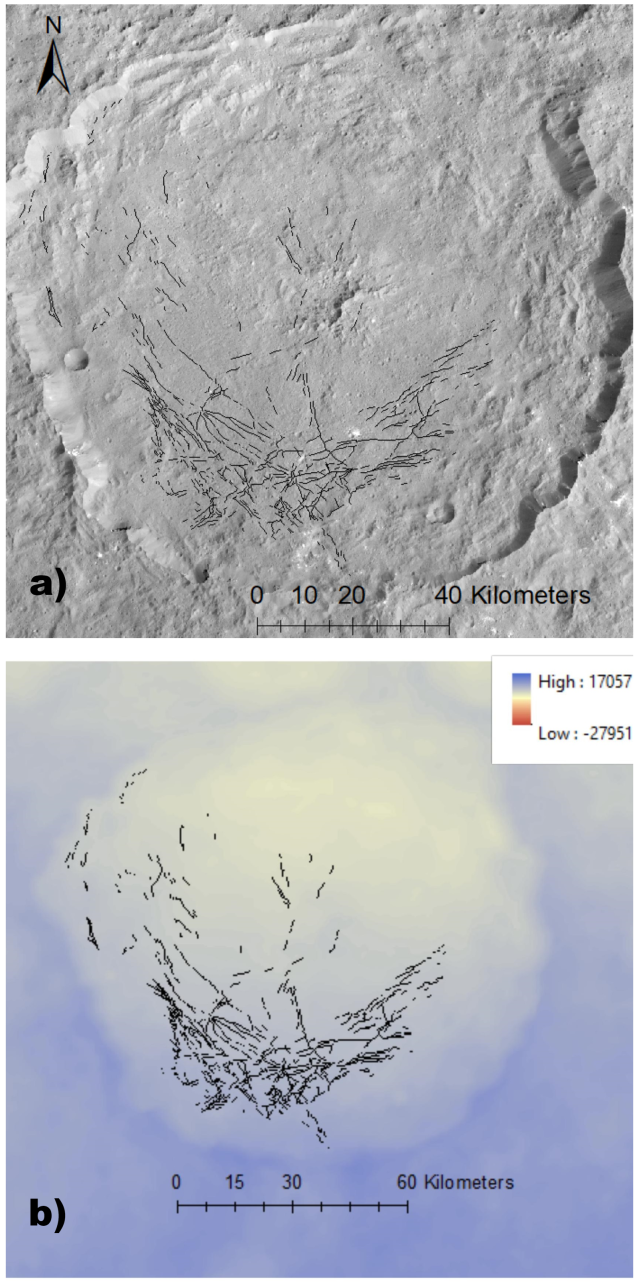

Figure 3.6:
a): The Dantu crater in LAMO view with fractures mapped in black.
b): The DTM image of Dantu crater with the fractures mapped in black.

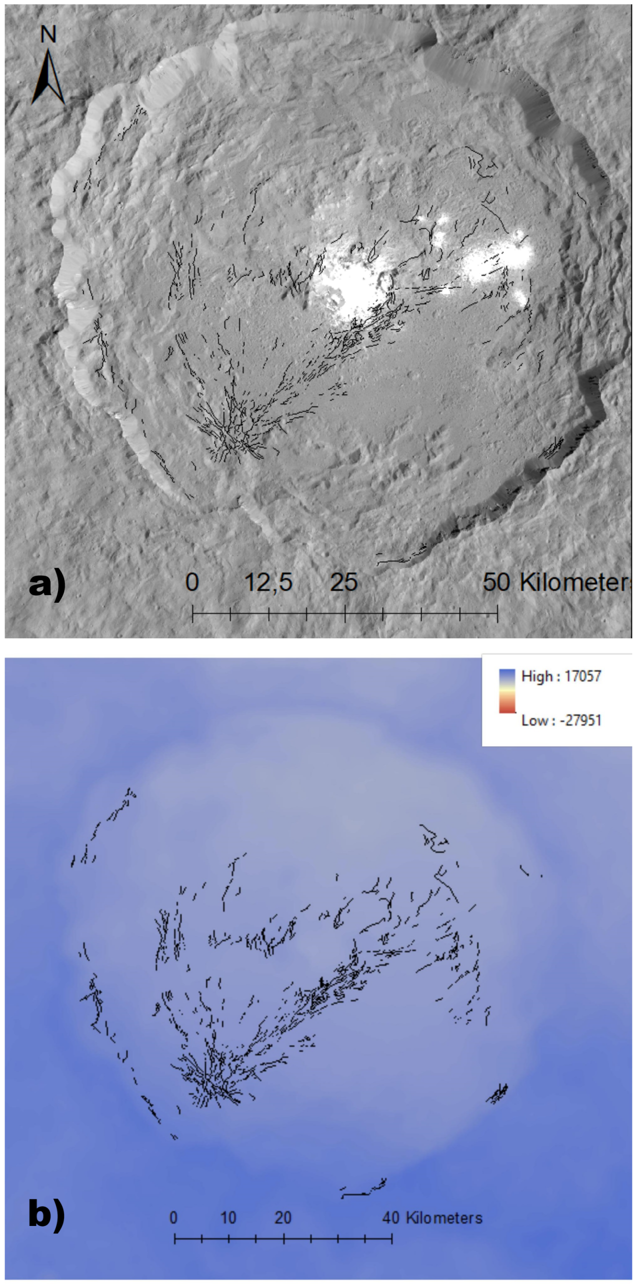

Figure 3.7:
a): The Occator crater in LAMO view with fractures mapped in black.
b): The DTM image of Occator crater with the fractures mapped in black.

3.3.1 Rose diagram analysis

The midpoint coordinates were useful for the calculations of the azimuthal angle between the vertical axis of the fracture and the Cerean parallel that passes by the midpoint. This was done to define a preferential angular distribution of the fractures.
This angular analysis was made with an extension of the ArcGis software named Polar Plots (J.Jenness, 2014). This program took the azimuthal angle calculated on the two sides of the intersection of the parallel and the fracture (this precaution was taken because the mapping was "homogeneus", indeed, not all the fractures where mapped from the top to the bottom or from left to right, so it was not correct to use just a single angle). Then, the Polar Plots program weighted every combination of angles with the length of its specific fracture, returning a polar graph, the so-called rose diagram. This reveals if the fracture systems has or not a preferential distribution.

3.3.2 Length distribution analysis

We performed an analysis on the length of fractures in Python to understand which distribution fits our dataset. Specifically, we are interested in understanding if our distribution follows a power-law or an exponential trend in order to assess if fractures penetrate or not the entire Ceres shell. Those fractures following a power-law distribution are thought to be involved in the uplifting of subsurface material. After the extrapolation of the data in the txt file, we used the Numpy module of Python to turn it into an array, with the genfromtxt function, then the array was sorted in increasing order with the sort command. After this part we used the Powerlaw module (Jeff Alstott) to do a fit of the data, and this fit was then used to do a comparing between a power-law distribution and an exponential distribution (through the distribution_compare function). Then we derived the α parameter of the fit in power-law, as well as the x_{min} parameter to determine the cutoff from which the power-law distribution begins. Using the module Plvar (Jeff Alstott), we then calculated the relative error of the α parameter and the x_{min}. Using the Plpva module (Jeff Alstott), we calculated the goodness of fitting (GoF) and the p-value associated with the two distribution.
We used for our analysis the statistical method developed by Clauset et al. in 2007.
We used the Matplotlib.pyplot module to do the histograms of the distribution of lengths, in addition to the cumulative distribution. In the latter, we highlighted the x_{min} value of the powerlaw distribution with his associated error to assess if there is an effective change in slope around that value (Appendix A).

The Python modules used for the statistical evaluations are based on the methods developed by Clauset et al. in 2007. We report here these methods, remembering that our dataset of lengths are defined as continuous. For estimating the α parameter of the distributions, the Powerlaw module used the method of maximum likelihood, deriving so a maximum likelihood estimator (MLE). The calculus for this MLE for the alpha parameter is dictated by:

$$\hat{\alpha} = 1 + n\Big[\sum_{i=1}^{n} \ln(\frac{x_i}{x_{min}})\Big]^{-1} \tag{3.3}$$

Where α is written as $\hat{\alpha}$ to enlight the fact that this is an estimation of the true value. In the equation n indicates the total number of data in the dataset, x_i the i-th data of the dataset and x_{min} the cutoff value of the power-law (so, for each $i > 0$, $x_i > x_{min}$).
The standard error associated with $\hat{\alpha}$ is then derived from the width of the likelihood maximum (Clauset et al. 2007), and its calculated from the formula:

$$\sigma_{\hat{\alpha}} = \frac{\hat{\alpha} - 1}{\sqrt{n}} + O\Big(\frac{1}{n}\Big) \tag{3.4}$$

Where, again n is the total number of data in the dataset.

This method of the maximum likelihood estimators are guaranteed to be unbiased in the asymptotic limit of $n \to \infty$ (Clauset et al. 2007). So for finite datasets, like ours, the biases are present, but those biases decay as $O(1/n)$ for any choice of x_{min} (Clauset et al. 2007). So if $n > 50$ the estimates on the parameters are reliable, and $\hat{\alpha} \to \alpha$ (Clauset et al. 2007). That is our case, indeed the two distribution counted $n = 630$ for Dantu and $n = 832$ for Occator.

For the estimation of x_{min} the program choose the value of $\sim x_{min}$ (the $\sim$ means that this x_{min} is an estimation of the true value) that makes the probability distributions of the measured data and the best-fit power-law model as similar as possible above $\sim x_{min}$ (Clauset et al. 2007). In general, if the chosen $\sim x_{min}$ is higher than the true value x_{min}, then we are effectively reducing the size of our data set, which will make the probability distributions a poorer match because of statistical fluctuation. Conversely, if the chosen $\sim x_{min}$ is smaller than the true x_{min}, the distributions will differ because of the fundamental difference between the data and model by which we are describing it. In between lies the best estimate (Clauset et al. 2007). The measure that the module of Python uses for quantifying the distance between two distributions is the Kolmogorov-Smirnov (KS) statistic defined as follows:

$$D = \max_{x > x_{min}} |S(x) - P(x)| \tag{3.5}$$

Where S(x) is the Cumulative Distribution Function (CDF) of the data for the observations with value at least x_{min}, and P(x) is the CDF for the power-law model that best fits the data in the region $x = x_{min}$. The estimated value $\sim x_{min}$ is then the value of x_{min} that minimizes D (Clauset et al. 2007). To evaluate the error on x_{min}, given our datasets with n measures, the Powerlaw module generates a synthetic dataset with similar distribution to the original, estimating then, with the KS method, the x_{min}. Then the program repeated this process 1000 times and calculated the standard deviation of these estimates over the number of repetition, giving us the uncertainety values that we searched (Clauset et al. 2007).

To strengthen our case for the power-law it was important to rule out the case of a general exponential distribution in each dataset. The comparison between the power-law and exponential distribution is important because only fractures with length distributions that follows a power-law are thought to penetrate deep in the crust (Soliva and Schultz, 2008; Schultz et al., 2010). To do this comparison, we used the distribution_compare function of the Powerlaw module that uses the likelihood ratio test. This test compute the likelihood of the data under two competing distributions, then the one with the higher likelihood is the better fit (Clauset et al. 2007). Then the program took the logarithm of the ratio, this logarithm is then positive or negative depending on which distribution is better, or zero in the event of a tie (Clauset et al. 2007). The function then returned two values, the first is the result of the logarithm of the likelihood ratio, indicating which fit is better, then it spouted another value, the p-value, calculated in the manner developed by Vuong. The p-value tells us whether the observed sign of the log likelihood is statistically significant (Clauset et al. 2007). If this p-value is less than 0.1 then the sign is a reliable indicator of which model is the better fit to the data, viceversa, if this p-value is large, the sign is not reliable.

The next and last step that we did in the statistical analysis part is to test the powerlaw hypothesis, calculating the goodness of fitting (GoF) and the p-value to quantify the plausibility of the hypothesis. Such tests are based on measurement of the "distance" between the distribution of the empirical data and the hypothesized model (Clauset et al. 2007). The Plpva module (Jeff Alstott) then compared this distance with distance measurements for comparable synthetic datasets drawn from the same model, returning so the p-value defined to be the fraction of the synthetic distances that are larger then the empirical distance (Clauset et al. 2007). If p is large, which means ~ 1 because $0 < p < 1$, then the those difference between the empirical data and the model can be attributed to statistical fluctuations alone, thus giving credit to our hypothesis. Viceversa, if the p-value is small, the model is not a plausible fit to the data (Clauset et al. 2007).

Once the p-value is calculated, it is important to set a lower boundary of acceptance, we decided to use $p = 0.1$ as this boundary, as defined by Clauset et al. This means that p-values ≤ 0.1 are associated with hypothesis that are unplausible, and so need to be discarded.

Chapter 4

Results and Discussion

The results coming from the analysis previous explained is here reported for Dantu and Occator crater, respectively.

4.1 Dantu's results

We mapped 630 fractures located on the floor of the Dantu crater with a length ranging from 150.418 m to 14396.803 m. The histogram of the fracture lengths distribution is shown in Figure 4.1.
The angular analysis made with the Polar Plots (J.Jenness 2014) module of ArcMap, reveal that the fractures of Dantu crater have one preferential direction in their distribution, which is from 150° to 330°, plus one minor direction from ~75° to ~255°. Therefore, the Dantu fractures show a NW-SE trend and a NE-SW trend, as shown in Figure 4.2. Thus the fractures are not randomly distributed, but it is clear that they have a preferential orientation.
The Python modules gave us the value of α to be 3.427 $\pm$ 0.306 and, for the x_{min}, a value of 2431.403 $\pm$ 341.259 m. Those can be assumed as the real values of the distribution, because the number of datas that have $x \geq x_{min}$ (n_{tail}) is about 170 $\pm$ 41, so greater than 50. In Chapter 2 we reported that for Clauset et al. this is the minimum value to accept the approximation in which the "hatted" values tend to be the true values. From the DistributionCompare function, we found that the the powerlaw is the best fit, when compared to the exponential distribution, of the data above x_{min}. Indeed we obtained a p-value of 0.262 for the comparison, well below the limit value of 0.5.
Finally, the Plpva module (J.Alstott), gave us a level of confidentiality. Indeed, the p-value found for Dantu is equal to 0.795, meaning that the powerlaw model for the cumulative distribution of the fractures is a plausible hypothesis. The cumulative distribution is shown in figure 4.3.

N° of fractures [ ]	630
α [ ]	3.427
σ_α [ ]	0.306
$\mathbf{x_{min}}$ **[m]**	2431.403
$\sigma_{\mathbf{x_{min}}}$ **[m]**	341.259
$\mathbf{n_{tail}}$ [ ]	170.670
$\sigma_{\mathbf{n_{tail}}}$ [ ]	41.018
p-value [ ]	0.795
GoF [ ]	0.034

Table 3.1: Resulting parameters for the distribution of lengths associated with the Dantu crater.

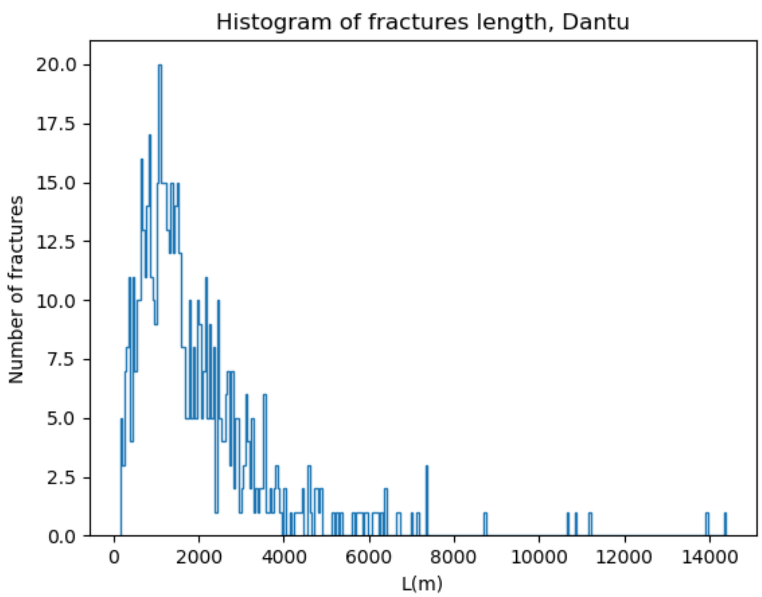

Figure 4.1: The histogram of the single fracture lengths of Dantu, the x-axis is binned 300 times.

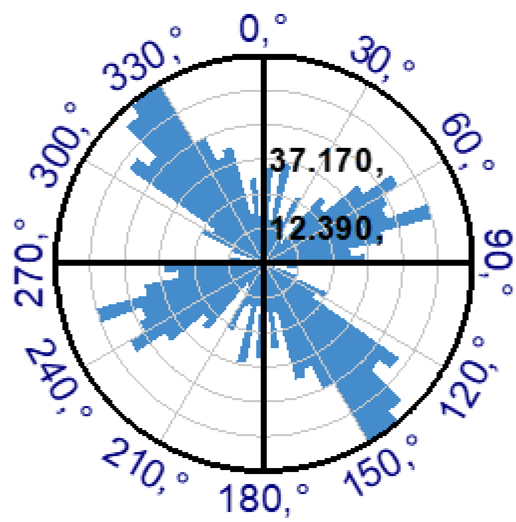

Figure 4.2: The rose plot of the azimuthal angles of the fractures of Dantu; the plot is radially symmetric due to the double counting of the angle.

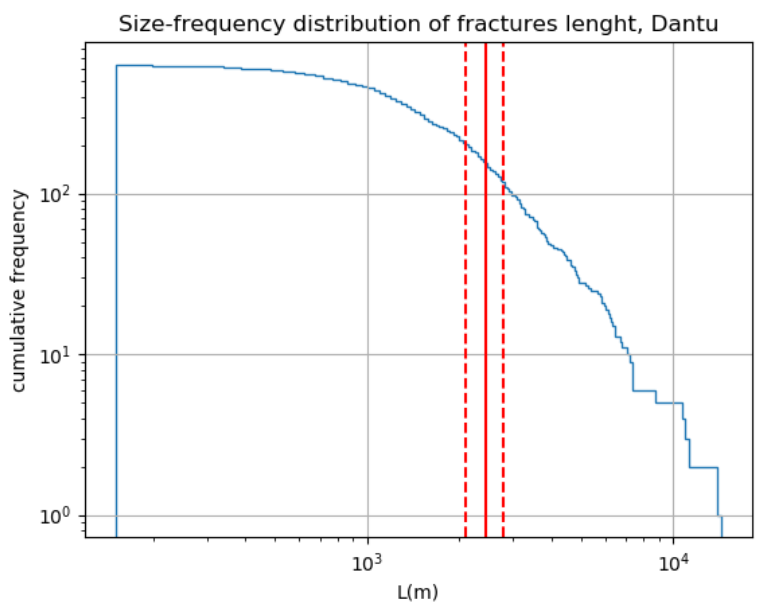

Figure 4.3: The cumulative histogram of the fractures length distribution of Dantu, the cutoff (x_{min}) is visible in red with its error dotted, that marks the passage from an exponential-kind of distribution, in the left part, to a power-law distribution, in the right part of the graph. The x-axis is binned 300 times.

4.2 Occator's results

We mapped 832 fractures located on the floor of Occator with a length ranging from 110.550 m to 7929.309 m. The histogram of fractures length distribution is shown in Figure 4.4.
The angular analysis made with the Polar Plots (J.Jenness 2014) module of ArcMap reveal that the fractures of Occator crater have just one preferential direction of distribution in the direction , which is from ∼50° to ∼230°. Therefore, the Occator fractures show a NE-SW trend, as shown if figure 4.5 meaning that the fractures are not randomly distributed.
The Python modules gave us the value of α to be 3.375 ± 0.469 and, for the x_{min}, a value of 1224.230 ± 385.216 m. Those can be assumed as the real values of the distribution, because the number of datas that have $x \geq x_{min}$ (n_{tail}) is about 222 ± 73, so greater than 50. For the same reasons explained in the previous section, this is the minimum value to accept the approximation in which the "hatted" values tend to be the true values. From the Distribution_Compare function, we found that the the power-law is the best fit, when compared to the exponential distribution, of the data above x_{min}. Indeed we obtained a p-value of 0.456 for the comparison. This value, in contrary to the distribution of Dantu, is almost at the limit of acceptancy, but we retained correct to infer that the power-law is in any case the best fit. Probably the rise of this p-value is caused by the rise of data avaliable in the Occator dataset with respect to the Dantu dataset.
Finally, the Plpva module (J.Alstott), gave us a level of confidentiality. Indeed, the p-value found for Occator is equal to 0.123 meaning that the our power-law model for the cumulative distribution of the fractures is indeed a plausible hypothesis, though not as strong as for the Dantu dataset of lengths. The cumulative distribution is shown in Figure 4.6.

N° of fractures [ ]	832
α [ ]	3.375
σ_α [ ]	0.469
$\mathbf{x_{min}}$ **[m]**	1224.230
$\sigma_{\mathbf{x_{min}}}$ **[m]**	385.216
$\mathbf{n_{tail}}$ [ ]	222.593
$\sigma_{\mathbf{n_{tail}}}$ [ ]	73.374
p-value [ ]	0.123
GoF [ ]	0.044

Table 3.2: Resulting parameters for the distribution of lengths associated with the Occator crater.

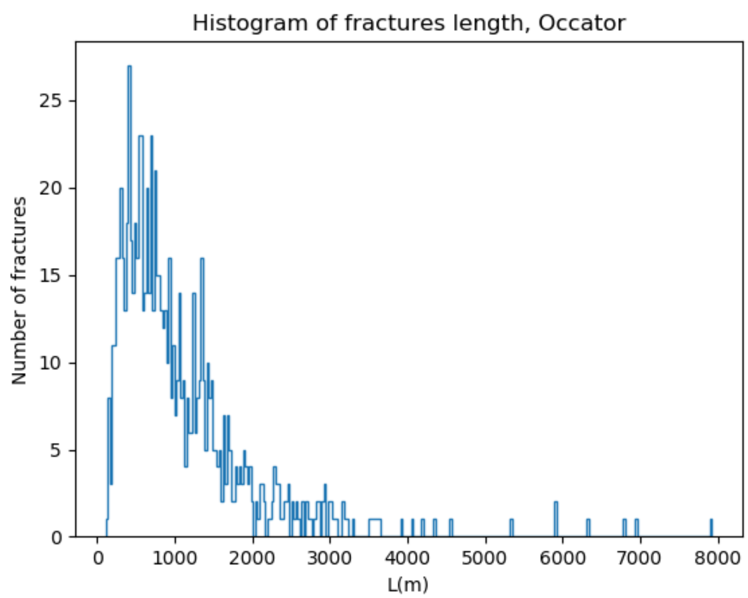

Figure 4.4: The histogram of the single fractures length of Occator, the x-axis is binned 300 times.

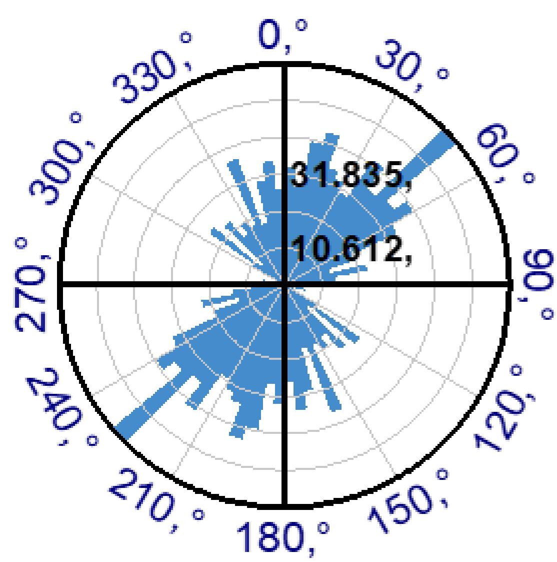

Figure 4.5: The rose plot of the azimuthal angles of the fractures of Occator; the plot is radially symmetric due to the double counting of the angle.

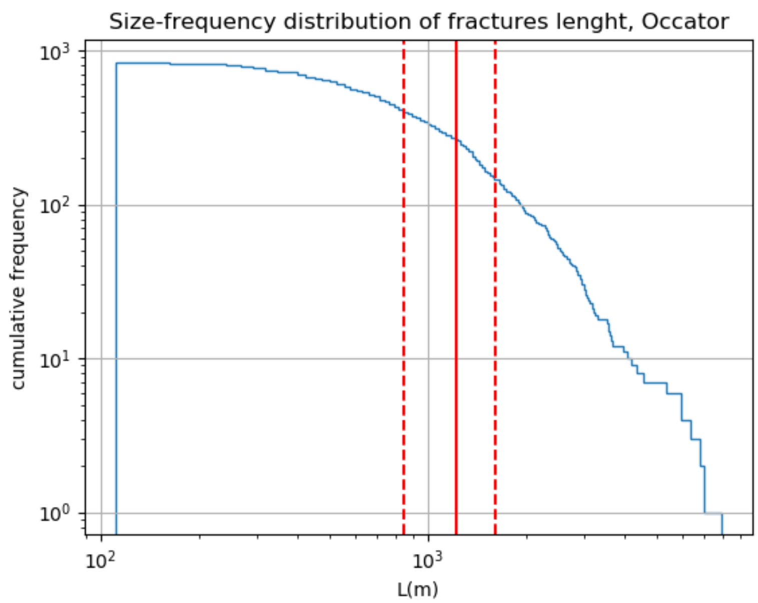

Figure 4.6: The cumulative histogram of the fractures length distribution of Occator; the cutoff (xmin) is visible in red with its error dotted, that marks the passage from an exponential-kind of distribution, in the left part, to a powerlaw distribution, in the right part of the graph. The x-axis is binned 300 times.

Chapter 5

Conclusions and future work

In this work, we analyzed the fracture systems located on the crater floors of Dantu and Occator. Specifically, we mapped the fractures deriving their length and orientation. From the analysis reported above, we found that fractures are not randomly distributed, but they have a preferential orientation. In the Dantu case, we obtained that fractures have a NW-SE trend, plus a minor NE-SW trend, while in the case of Occator, the fractures have NE-SW orientation. In addition, analyzing fractures length distribution, we found that the fractures follow both an exponential and power-law behaviour below and above a certain fracture length. Those fractures following a power-law behavior are the ones that can penetrate below the surface down to the mechanically discontinuity. Hence, we found that there are fractures able to penetrate the entire crust of Ceres in both craters cases. In the next future, it will be interesting to analyze in greater detail these type of fractures in order to quantify the thickness of the Ceres crust giving insights into the internal stratification of the body. Indeed, other technical applications like self-similar clustering (SSC), will allow us to infer how much in depth the fractures penetrate in the crust. This technique was already used on other Solar System bodies, as on Earth (Mazzarini and Isola, 2010), Mars (Pozzobon et al., 2015) and Enceladus (Lucchetti et al., 2017).
In addition, since Ceres hosts a certain number of Class I FFCs, it will be interesting to apply the same analysis also to other craters, such as Ezinu, Guae, Ikapati, Azacca, Haulani and Kupalo. This will enlarge the statistic and characterize entirely the behaviour of this category of peculiar craters, the FFC craters.

Appendix A

Codes

```
#import of the modules
import powerlaw as pl
import numpy as np
import matplotlib.pyplot as plt
from numpy import log
import plvar as pv
import plpva as pp

#generating the ordered arrays of fractures lengths
dantu = np.genfromtxt("dantulsp.txt")
d = dantu[::-1]
g = np.genfromtxt("occatorlsp.txt")
occator = np.sort(g)
o = occator[::-1]

#fitting the data to the theorical distributions
z=pl.Fit(dantu)
w=pl.Fit(occator)

#comparing between the powerlaw and the exponential
q=w.distribution_compare('power_law', 'exponential')
p=z.distribution_compare('power_law', 'exponential')
print p
print q

#finding alpha and xmin parameter for the distributions
alpha_d=z.power_law.alpha
xmin_d=z.power_law.xmin
print alpha_d
print xmin_d
```

```
alpha_o=w.power_law.alpha
xmin_o=w.power_law.xmin
print lpha_o
print xmin_o

#finding the errors on alpha and xmin, also finding ntail with its
#error, the p-values and the GoF of the distributions
err_d = pv.plvar(d)
err_o = pv.plvar(o)
p_d = pp.plpva(d, xmin_d)
p_o = pp.plpva(o, xmin_d)
#here we putted the complete list of fractures
#because, somehow, numpy and plvar or plpva
#do not get along
print err_d
print err_o
print p_d
print p_o

#doing the cumulative histograms of the distributions
#enlightening the cutoff value of xmin
plt.hist(d, bins=300, cumulative=-1, histtype='step')
plt.xscale('log')
plt.yscale('log')
plt.title('Size-frequency distribution of fractures lenght, Dantu')
plt.xlabel('L(m)')
plt.ylabel('cumulative frequency')
plt.axvline(x=xmin_d, color='r', label='xmin')
plt.axvline(x=xmin_d+342.0687, color='r', ls='--')
plt.axvline(x=xmin_d-342.0687, color='r', ls='--')
plt.grid(True)
plt.show()

plt.hist(o, bins=300, cumulative=-1, histtype='step')
plt.xscale('log')
plt.yscale('log')
plt.title('Size-frequency distribution of fractures lenght, Occator')
plt.xlabel('L(m)')
plt.ylabel('cumulative frequency')
plt.axvline(x=xmin_o, color='r', label='xmin')
plt.axvline(x=xmin_o+379.7369, color='r', ls='--')
plt.axvline(x=xmin_o-379.7369, color='r', ls='--')
plt.grid(True)
plt.show()
```

Appendix B

Tables

B.1 Dantu's fractures lengths [m]

150.4177293	158.7503175	167.3375275	187.0890434	188.5450112
199.8111859	221.8211697	243.2157564	246.8427945	258.8573158
261.2030634	270.3119184	282.4494311	283.4887141	286.6649733
296.2375965	299.2192147	301.7526035	320.2448575	320.2764109
322.4735172	329.2767163	329.332633	340.9085037	351.2554812
351.5706298	358.2635969	360.4560657	365.9014025	372.5591615
381.3313484	381.7745501	382.6461803	386.312822	392.7938623
393.7235466	411.8005808	413.4660329	440.0849719	450.4505479
451.6692713	454.5879306	461.8491237	462.4564586	465.4106722
472.8667099	474.6893013	478.0403124	479.7684818	488.1760251
496.0947422	497.1959527	519.4371003	523.3808081	523.4556548
527.4389194	534.1514809	534.1686393	541.7124357	543.9831115
545.2822422	552.1465462	562.2407078	562.2827782	564.8621134
576.853058	582.8858018	584.8864061	596.4609526	602.4688156
605.3911245	606.1685005	612.2258175	613.834561	613.834561
621.6049303	628.3973306	629.019963	638.0306299	638.412398
642.2950784	649.5897997	654.7849242	655.9142246	656.0547444
658.3517628	658.777396	662.3314071	663.4002293	664.7587274
669.6768615	670.4803367	675.3473937	678.8023265	679.8087056
682.031305	689.2256745	691.0624092	697.0871602	703.7327026
705.0617747	707.2361784	709.1940301	710.3860751	718.5324785
720.7208767	722.2187216	722.3486318	722.4897903	728.3568927
730.9859581	732.6854355	736.4659407	748.516319	755.6289991
767.300329	771.7145235	785.8301099	786.678062	788.3402256
790.4719649	790.769417	791.8655744	796.0552732	797.0148745
801.8186	807.1280775	810.1772297	811.031408	811.2248904
818.4807314	822.0538039	830.4266926	831.0716723	834.3836414
834.779752	835.1565585	836.3445485	840.9080515	842.8898763

846.4107357	847.2634646	848.9793125	850.7451409	854.186669
858.6245731	858.6245731	869.4010916	871.7810443	873.0792917
879.0036006	879.1771174	886.4300486	886.7772475	896.3634927
897.3473525	905.394396	910.0048749	910.8590082	911.6342088
927.2124922	927.2711301	928.3563763	941.1545892	942.8576675
946.5979275	952.2543751	957.120068	958.7286709	959.4212021
965.4059822	968.2343764	970.5344548	971.1632361	977.2233693
982.356671	1000.85808	1005.31516	1008.21201	1010.609238
1015.761715	1018.110651	1020.302496	1021.037714	1022.632993
1026.305284	1030.860629	1032.376064	1040.406863	1041.95283
1044.039397	1048.93095	1056.945495	1057.094486	1058.077894
1060.813566	1061.321548	1061.723961	1061.870853	1062.957407
1064.208112	1067.943668	1068.876644	1074.07622	1074.500442
1078.859794	1086.191554	1089.562638	1090.588886	1097.272167
1097.562198	1097.687035	1103.04266	1103.824592	1105.745313
1109.105848	1112.250634	1113.617642	1114.048228	1114.834277
1116.538356	1124.711069	1131.742995	1132.257699	1134.974573
1136.440072	1147.060488	1148.322912	1148.383238	1154.192597
1154.235696	1154.863851	1156.696009	1165.152434	1167.81934
1168.58525	1172.145552	1174.984102	1178.014203	1187.191464
1189.336872	1190.954391	1201.095497	1203.382986	1205.33323
1207.287466	1208.723431	1209.134259	1218.846735	1218.932479
1219.671342	1226.702641	1227.701367	1229.772259	1234.567219
1236.179346	1238.321731	1243.322398	1249.55726	1263.695016
1264.994036	1268.141334	1269.418048	1272.293534	1274.764829
1280.602365	1281.049695	1281.851641	1288.079106	1289.770694
1299.88877	1309.118674	1309.118851	1313.024857	1316.926737
1322.484821	1328.009032	1328.943974	1331.879517	1333.832023
1334.499925	1336.760217	1338.217244	1339.455804	1341.387452
1345.026283	1350.348935	1355.202011	1356.630918	1360.993817
1363.259249	1363.591258	1375.10297	1377.424913	1377.850024
1378.393684	1384.73578	1396.461495	1397.269579	1405.463236
1407.235764	1409.93163	1413.457576	1417.438024	1421.253046
1421.834819	1425.397437	1428.060749	1430.7437	1439.384031
1443.636108	1445.582823	1453.045487	1454.832533	1458.689661
1461.96052	1467.051712	1469.351843	1469.917183	1477.0493
1477.401313	1477.460394	1480.046686	1480.240735	1480.961073
1480.9826	1481.151187	1485.924282	1489.214309	1497.014224
1500.946219	1508.045468	1511.031623	1513.432305	1514.075881
1517.397678	1523.883954	1527.41603	1530.10918	1534.928934
1543.099641	1544.707768	1547.991455	1551.674429	1560.061263
1562.613566	1566.272634	1568.244163	1572.676541	1575.047862
1586.572082	1587.381167	1587.647266	1593.230977	1595.933423
1601.288048	1607.105364	1619.874066	1625.640093	1632.243953
1632.875474	1642.507018	1642.698916	1657.600772	1660.699328
1666.265058	1674.142257	1678.719286	1679.110325	1695.536127

1699.165381	1727.060845	1729.388137	1734.382392	1748.609508
1749.375367	1769.08117	1769.731484	1769.974229	1770.346911
1771.254255	1773.07777	1778.277158	1783.283173	1800.236247
1811.169954	1830.414502	1835.837839	1844.950101	1851.244119
1852.478137	1865.162848	1867.262601	1867.452437	1869.978054
1882.704764	1885.90186	1897.501024	1897.703236	1913.688481
1922.481127	1927.040544	1931.490857	1939.529183	1956.78099
1957.774741	1971.697083	1976.472783	1980.700262	1988.86626
1990.125633	1994.979189	1999.341197	1999.440155	2003.175922
2007.076982	2008.456715	2013.321316	2028.825658	2032.219513
2045.75503	2046.285503	2048.838061	2057.318732	2061.900635
2066.451042	2069.568	2081.251501	2101.727349	2118.400267
2119.381357	2124.420202	2136.197074	2137.577295	2143.449978
2148.821276	2154.191414	2156.365734	2159.497122	2159.632025
2159.669053	2167.310041	2183.175593	2185.47357	2190.537887
2190.991889	2196.829687	2206.806414	2219.650981	2233.295322
2236.077417	2244.844879	2249.830138	2271.686146	2273.206352
2274.536656	2277.79806	2278.955939	2279.951596	2285.795092
2306.041939	2314.2941	2316.977866	2317.765125	2320.543126
2338.526258	2342.181408	2343.988674	2345.536627	2347.081387
2359.020245	2375.98496	2377.798767	2415.803112	2431.402743
2432.876641	2433.151071	2436.270074	2445.12498	2445.71068
2448.966848	2459.831588	2462.161478	2466.49341	2482.344896
2483.9636	2486.04191	2492.434577	2497.638549	2549.095913
2555.387205	2570.233644	2571.227249	2574.995742	2605.672779
2614.61052	2618.293349	2635.402886	2644.119776	2648.664074
2651.636772	2661.713491	2662.895686	2673.553428	2677.069687
2687.326868	2689.41035	2689.434064	2698.883772	2701.863148
2719.312691	2721.9973	2729.982465	2779.818419	2784.433324
2786.610853	2800.05756	2805.472992	2805.688011	2806.290128
2848.616127	2854.138124	2857.968186	2858.461741	2875.3174
2875.588561	2893.811424	2908.702053	2911.213667	2915.852414
2943.544688	2946.925077	2983.304779	3025.045274	3026.245238
3049.601499	3054.654782	3055.043081	3096.742328	3098.908163
3105.462303	3113.996189	3132.788627	3141.170854	3147.812671
3160.320183	3176.743853	3176.958818	3207.400056	3219.775717
3237.707185	3240.914837	3255.993971	3266.141222	3271.093086
3304.165555	3370.675168	3377.27017	3384.997308	3443.271081
3455.960591	3498.616789	3516.829645	3529.341689	3538.974368
3554.291088	3564.454883	3566.476798	3566.97679	3608.383917
3620.957871	3666.708641	3673.418672	3734.054406	3789.332343
3802.24853	3819.286387	3831.659652	3846.064932	3872.344393
3901.026997	3940.63738	4032.886834	4036.356351	4151.528644
4246.915845	4317.962599	4330.649753	4413.570098	4444.134952
4450.931182	4572.592696	4576.480393	4609.804449	4617.755102
4718.036374	4721.130227	4776.489702	4801.22699	4838.406961

4876.307915	4881.626825	5144.612136	5277.563389	5361.745358
5647.30347	5743.863172	5793.622935	5845.577483	5941.258718
5976.707585	6104.940137	6163.024522	6228.816109	6276.755529
6380.745852	6383.733	6674.432153	6743.045346	7005.30858
7164.522313	7343.188358	7350.777523	7355.803106	8740.949562
10668.97584	10856.15485	11202.76977	13955.35448	14396.80306

B.2 Occator's fractures lengths [m]

110.54984131	143.00144043	143.27216154	146.698346	151.02211859
153.45694185	154.09596752	154.8247639	162.45535341	170.13569183
174.54515391	179.44495227	191.12280211	195.38262641	199.12615024
201.09671663	203.64080279	206.70345515	209.17190941	210.07358862
210.79625119	212.83653034	213.89985362	214.97438828	217.7333254
217.80719692	220.62431314	224.89628313	225.62659391	230.32667305
231.81614871	237.83131249	238.49267073	238.78693591	248.11580458
251.56346465	251.91189313	253.17578964	253.27179246	254.88092835
254.88092835	255.24116001	256.47065031	259.82827733	262.05826167
262.59198577	264.03575928	264.91438588	264.91438588	266.06593504
270.24924741	270.49406355	271.97116907	272.88645584	273.12437348
274.86440477	275.18834643	275.2816766	275.40606408	277.65078683
278.12452961	280.13610754	284.49508291	289.64970211	290.54210459
291.12426901	294.24677018	296.63531667	298.42845683	299.77034609
300.13276348	300.85422892	301.34541683	302.01414925	303.25761172
303.45662737	308.93200861	310.0278483	311.30953061	312.87467757
312.89347081	313.18494592	313.71575651	314.30959286	316.49854959
317.29249336	322.41100159	322.81745938	323.4043405	324.46918541
327.27216358	327.64820417	328.3194345	331.19516836	333.84780361
335.37931175	335.39153129	337.46232672	340.08435387	341.7369253
343.62129727	343.91109627	347.28520476	352.28953163	357.18959241
358.32314199	358.4902809	361.79256086	363.26121353	364.72388223
364.96025899	365.98395074	367.90481061	369.5054236	369.70754832
371.61142576	372.05770946	372.82861218	373.6538702	374.411875
376.66936183	380.13597366	380.69639842	381.61361357	384.54526704
384.77628594	387.96906952	389.11650595	392.63322215	393.68312252
395.6009096	396.54541303	396.82121387	397.79325094	399.56862299
401.18203373	401.34678539	402.33773366	402.44357107	402.7976007
403.70720408	404.29887489	404.55693056	405.3624979	405.39707
409.20141911	409.74100489	411.66392216	412.00637102	413.29320527
413.41228516	415.56428197	415.57630202	415.94400897	417.52088776
417.96938769	419.61753183	420.4715111	421.0542731	421.88475571
425.18028123	425.8314643	425.97180166	427.40592448	427.98853073
431.69610902	432.67874304	433.9175345	434.22939861	436.45130988
436.95529976	441.23138202	441.59355781	446.30441816	447.32673367
448.34975908	448.39137017	449.98707115	450.44825631	451.35837566
454.25234016	457.94260972	458.32660965	458.57095027	460.74831638
463.61705693	466.46036284	467.72260842	468.66458863	469.8326065
475.32997277	476.98534145	477.57203951	478.69209688	479.86244014
482.62654245	483.10743863	483.3651591	486.35280306	487.04072856
487.16014027	489.63859815	490.74636856	492.02027594	495.50897906
496.97024601	497.16271921	500.42814643	501.42982328	505.14078901
505.57781482	506.1091361	512.23726144	514.7457074	516.75014265

517.20424864	518.31848421	522.0861455	522.85785821	523.19853774
523.42017749	523.92988329	524.11966671	525.82553045	525.96177717
528.07151856	528.70850198	528.73010065	528.77907809	530.23336903
530.80822031	531.64189927	534.69141125	535.53057516	535.73580281
536.78832734	538.64549541	540.94546121	542.31983435	543.83501153
544.41537495	546.51862752	548.64737759	549.60449137	549.61683282
549.68837428	549.69844513	551.33647906	554.83248104	555.39927878
556.12992063	556.5325166	561.06328852	561.08275475	561.64824387
561.7062144	561.82374826	562.85688733	562.92913122	563.15432934
564.56527618	566.19053109	568.60415264	568.60980074	570.12644457
570.2093007	570.25225062	571.936332	575.10659105	575.23720256
576.82582161	582.80799649	585.78548199	586.1762594	587.3057364
589.01348576	593.25993385	596.96733977	600.13616793	601.28560605
602.50124363	603.59615295	604.67605452	604.84744699	606.47537767
606.72629003	608.54288375	613.74745626	616.74555146	617.61313145
620.43445261	623.20801448	628.15035561	628.6042212	629.2564132
629.48872291	629.82883511	631.10510439	632.88975888	633.05331764
634.29532062	637.65988191	637.91498144	638.23712815	638.41239798
640.76410525	640.99160408	641.99874043	646.10861429	646.20241416
647.4763774	648.30639155	649.76368118	652.046422	652.89658728
656.15578623	657.11110439	657.23398351	658.55371925	661.57681828
665.16996077	665.40377271	667.11840605	667.17642206	670.18226818
670.62872055	671.44192113	673.54546039	675.32118489	679.21393377
680.26872813	680.77451197	684.32660911	685.7876632	686.27867527
687.14339326	690.47660022	691.40880117	692.05783962	692.1391106
692.69190284	695.9434714	696.1775682	696.71511136	697.29268363
700.08659343	700.12309726	701.21985946	704.74112006	704.96581506
706.40674344	707.79274085	708.14972325	708.20067464	709.16372736
711.68655319	714.07980173	715.64266659	716.5162511	721.06442031
722.30838291	726.28775252	727.72587733	728.97733072	730.0722521
730.62076236	731.01900864	731.06470627	741.24336224	741.51486138
742.58090668	743.62658414	744.1288897	745.21248811	745.66514446
747.21457006	747.22274798	749.92188853	750.04805717	750.72757009
750.74709385	751.66796107	751.88608114	754.35433937	755.20585534
755.23812182	756.39770227	760.25371738	760.50334625	763.77753711
765.87536646	769.62201705	770.95039233	775.79420998	776.78614871
776.99376948	779.30220345	780.75399707	782.42933627	782.96855082
785.31057739	785.40191077	787.34152498	787.54033561	789.3822902
791.7773457	793.2643259	796.55944575	800.26076083	801.52308826
802.33408087	805.02278429	806.50607232	806.84736112	808.26066603
808.97665821	810.02426205	811.48266133	811.6637357	817.16628655
817.40841027	819.09140139	820.93474606	826.87530336	827.32716333
829.3850963	829.77732514	830.77363052	833.50087523	836.50492533
837.01953232	837.96233207	842.78879247	843.71984996	844.14150462
847.47646109	859.90110703	860.34102899	860.37609058	860.62465108
863.57594722	864.62209966	865.4383148	866.33828247	867.43212026

868.79918071	869.61193112	876.03758961	876.35117909	876.88970546
881.10781025	884.0249398	884.61098977	886.95923858	887.96372842
889.33310384	891.32958821	892.49532795	896.31959423	896.37750369
899.68240072	900.02081219	902.17086597	903.5417968	904.41209743
909.47522549	909.56334171	918.66295276	920.59978963	920.76796247
927.99681091	928.34896121	929.5073788	930.64460461	934.23958956
935.50481341	936.48995145	938.91357831	940.24581503	940.59042337
941.571176	942.01046368	944.07353393	945.58855136	946.90177164
949.64157906	951.029576	959.01705793	962.00310212	965.82170479
968.13003483	974.77921449	976.28829579	976.66931771	979.91096894
981.3426861	981.47170826	985.52106731	985.61970376	985.94174689
986.63792453	992.89420842	999.05630784	1006.02703484	1007.98661866
1009.85634607	1010.53025545	1013.77352358	1019.0979074	1023.98702533
1024.31768702	1025.72210146	1027.26525876	1031.53529146	1039.86188693
1042.56500274	1045.23155996	1045.40752171	1049.14323248	1050.12989015
1050.56731344	1051.52630322	1055.08144702	1055.28780458	1059.15125708
1064.21418472	1064.33095436	1064.95644308	1066.32220572	1066.85237151
1073.34006083	1073.95183607	1079.74842396	1080.30804219	1084.22046021
1087.00933621	1087.41939819	1087.86454764	1096.04477537	1099.47356053
1101.3269338	1103.19937706	1107.70719382	1111.24174312	1111.45580151
1111.89435019	1114.06525367	1114.59924556	1123.60003365	1128.51634624
1138.38724998	1139.09901914	1150.37569608	1158.05071419	1161.18117411
1161.51309678	1162.68994636	1168.69251675	1170.24976373	1170.35459977
1174.69620628	1180.26112571	1189.44139623	1195.54414193	1202.31748227
1202.89775776	1203.80338899	1205.29011253	1208.25447218	1224.23031696
1227.53247977	1228.50897375	1230.83050665	1232.07743395	1235.28839768
1235.98480038	1236.90881869	1239.12355994	1241.27161913	1241.80093265
1241.8973091	1242.97388409	1244.25290708	1247.73885792	1248.07885379
1250.80831037	1252.3882357	1270.35455066	1271.41476325	1272.4418982
1276.86939883	1277.22410165	1281.5879993	1285.636078	1286.69784269
1300.15302381	1300.50066682	1305.52650469	1307.21882451	1307.6203541
1308.29218672	1309.8146821	1316.07513031	1318.66733668	1321.07732614
1322.94581081	1327.63884968	1328.09883556	1328.34305387	1333.59227849
1335.70570668	1336.28826865	1337.24139358	1339.86405013	1339.98735956
1340.99632142	1341.95458455	1346.08339276	1346.78690006	1346.86602004
1348.6131215	1352.44412232	1352.55933004	1353.29969339	1356.19185681
1361.43166246	1363.2794977	1365.85497885	1366.93882807	1368.34871066
1372.27665684	1374.34581036	1376.85569177	1380.6863456	1382.95499223
1392.44804333	1402.52006379	1403.24975381	1403.45514777	1403.8781394
1415.04659203	1417.10178153	1420.3823844	1421.031458	1424.28888151
1425.24216024	1429.30706537	1431.59310056	1432.94946397	1435.45522177
1442.49431617	1446.87065136	1449.27932912	1449.54519297	1453.00494044
1464.72277652	1465.31165924	1465.47373506	1477.30755549	1477.57623131
1481.10987516	1481.13192492	1483.24238102	1485.84215902	1485.94015501
1487.74436968	1491.38441038	1505.81910523	1507.93230309	1512.02345625
1513.32734372	1517.75547323	1520.61849595	1525.39537785	1530.35206676

1531.5326829	1532.12598443	1545.36999783	1546.29453808	1546.92595699
1564.2845611	1573.0345175	1578.04545127	1588.58292053	1591.12768142
1593.54063793	1598.58915371	1600.43292033	1630.26245711	1633.50510927
1638.37572927	1641.42954272	1643.20827981	1646.40977456	1648.00656714
1654.39276028	1668.03473295	1670.83156945	1676.00325007	1676.19490684
1677.76835189	1680.66116809	1681.62604411	1690.12580396	1699.80512809
1702.93830525	1704.08854485	1712.03914908	1716.75483133	1720.48454241
1733.67786964	1746.89351076	1756.17559498	1756.2912035	1780.27335683
1797.41498561	1800.66570159	1800.765742	1810.23045575	1818.96289954
1823.66180895	1844.24277617	1847.38566074	1852.8595334	1853.38996442
1860.65302474	1869.82887132	1874.67965294	1893.14913043	1900.73412763
1904.4806935	1905.26383782	1906.53604148	1909.39849718	1912.96493371
1922.82946516	1929.94695173	1949.83642156	1953.57991495	1957.60519299
1964.57193661	1966.54822285	1972.73837211	1983.75766207	2004.12274113
2012.67421414	2055.48775662	2061.98937952	2091.23338173	2102.46344101
2114.2258764	2116.67297327	2127.43083958	2131.18823494	2141.87763876
2165.83474729	2169.39441643	2220.43104896	2226.73027202	2248.2818945
2273.49277181	2280.49965552	2286.30635369	2292.83674358	2295.93803589
2300.25710347	2300.3407118	2307.36716312	2334.3428212	2341.22356857
2348.18935143	2365.33312696	2382.27575906	2416.25152884	2428.07264289
2451.71653841	2453.57945092	2456.82309563	2480.22897514	2480.75274303
2513.35720094	2527.00351238	2557.23503939	2577.01244198	2577.8625463
2592.95725602	2639.14837059	2645.59180744	2712.31394138	2713.42547786
2739.32179027	2753.55124542	2816.50947545	2822.94557538	2828.94565823
2865.27388329	2870.38721076	2915.76028209	2924.37684456	2931.78970345
2939.29062342	2939.33526798	2981.61164417	2994.31208679	3014.09110519
3020.05966229	3050.04007405	3079.46139884	3083.98686902	3180.3424135
3180.38572976	3205.30553944	3221.00133948	3307.31779462	3509.26407357
3550.49999606	3555.65436155	3586.49636017	3616.4501463	3640.53948605
3927.08163244	4055.83643213	4179.36888715	4347.50955825	4566.88109959
5323.06087983	5906.52425169	5915.37018601	6314.43040201	6787.84425153
6942.67887095	7929.30932145			

Bibliography

- Alstott et al. 2014. Powerlaw: a Pyton package for analysis of heavy-tailed distributions. 'PLos ONE 9(1):e85777 http://www.plosone.org/article/info%3Adoi%2F10.1371%2Fjournal.pone.0085777.

- Bland M.T et al. 2016. Composition and structure of the shallow subsurface of Ceres revealed by crater morphology. DOI: 10.1038/NGEO2743

- Buczkowski, D.L. et al. 2016. The geomorphology of Ceres. Science 353. doi:10. 1126/science.aaf4332.

- Buczkowski et al., 2018. The geology of the occator quadrangle of dwarf planet Ceres: Floor-fractured craters and other geomorphic evidence of cryomagmatism. Icarus 316 (2018) 128–139

- Clauset et al. 2007. Power-law distributions in empirical data. arXiv:0706.1062v2 [physics.data-an] 2 Feb 2009

- De Sanctis, M.C. et al. 2016 Bright carbonate deposits as evidence of aqueous alteration on (1) Ceres. Nature 536, 54–57. doi:10.1038/nature18290.

- Fu et al. 2017. The interior structure of Ceres as revealed by surface topography. Earth andPlanetaryScienceLetters476(2017)153–164

- Hisinger at al. 2016. Cratering on Ceres: Implications for its crust and evolution. http://science.sciencemag.org/content/353/6303/aaf4759

- J.Jenness 2014. Polar plots and circular statystics. Jenness Enterprises.

- Jozwiak et al. 2012. Lunar floor-fractured craters: Classification, distribution, origin and implications for magmatism and shallow crustal structure. https://doi.org/10.1029/2012JE004134

Jozwiak et al. , 2015. Lunar floor-fractured craters as magmatic intrusions: Geometry, modes of emplacement, associated tectonic and volcanic features, and implications for gravity anomalies. https://doi.org/10.1016/j.icarus.2014.10.052

- Kallish et al. 2017. Geological evolution and composition of the Dantu crater. EPSC abstract vol. 11 Epsc2017-596, 2017

- Krohn et al. 2016. Cryogenic flow features on Ceres: Implications for crater-related cryovolcanism. Geophysical Research Letters RESEARCH LETTER 10.1002/2016GL070370

- Krohn et al. 2018. Ring-Mold Craters on Ceres: Evidence for Shallow Subsurface Water Ice Sources. Geophysical Research Letters RESEARCH LETTER 10.1029/2018GL078697

- Lucchetti A. et al. 2017. Brittle ice shell thickness of Enceladus from fracture distribution analysis. Icarus 297 (2017) 252–264

- Mastrodemos N. et al. (???). Optical navigation group, mission design and navigation section, Jet Propulsion Laboratory, California Institute of Technology, Pasadena, CA, 91109 .

- Mazzarini, F., D'Orazio, M., 2003. Spatial distribution of cones and satellite-detected lineaments in the Pali Aike Volcanic Field (southernmost Patagonia): Insights into the tectonic setting of a Neogene rift system. J. Volcanol. Geotherm. Res. 125, 291–305. doi: 10.1016/S0377-0273(03)00120-3 .

- Mazzarini, F., 2004. Volcanic vent self-similar clustering and crustal thickness in the northern Main Ethiopian Rift. Geophys. Res. Lett. 31, L04604. doi: 10.1029/ 2003GL018574

- Mazzarini, F., Isola I., 2010. Monogenetic vent self-similar clustering in extending continental crust: examples from the East African Rift system. Geosphere 6, 567–582. doi: 10.1130/GES00569.1

- Pozzobon R. et al., 2015. Self-similar clustering distribution of structural features on Ascraeus Mons (Mars): implications for magma chamber depth. Geol. Soc. London Spec. Publ. 401. doi: 10.1144/SP401.12

- Preusker, F., et al., 2016. Dawn at Ceres – Shape model and rotational state. In: Lunar Planet. Sci. Conf. XXXIV abstract 1954.

- Schenk, P. et al. 2015. Impact craters on Ceres: evidence for water-ice mantle? In: Euro. Planet. Sci. Congress abstract EPSC2015-400.

- Schultz 1976. Floor-fractured lunar craters. Schultz, P.H. The Moon (1976) 15: 241. https://doi.org/10.1007/BF00562240

- Schultz, R.A. et al. 2010. Fault populations. In: Thomas R.Watters, Richard, A.Schultz (Eds.), Planetary Tectonics. Cambridge University Press, Cambridge, pp. 457–510 .

- Scully et al. 2017. Evidence for the Interior Evolution of Ceres from Geologic Analysis of Fractures. Geophysical Research Letters RESEARCH LETTER 10.1002/2017GL075086

- Sierks, H. et al. 2011. The Dawn framing camera. Space Sci. Rev. 163, 263–327
- Soliva R., Schultz R.A., 2008. Distributed and localized faulting in extensional settings: insight from the North Ethiopian Rift–Afar transition area. Tectonics 27, TC2003. doi: 10.1029/2007TC002148 .

- NASA, 2015. Dawn at Ceres, press kit NASA

- Websites utilized:

  astrogeology.usgs.gov

  solarsystem.NASA.gov